

A novel imaging x-ray microscope based on a spherical crystal

M. Sanchez del Rio^{a)}

European Synchrotron Radiation Facility, BP 220, F-38043 Grenoble Cedex, France

L. Alianelli

*INFM-OGG c/o ESRF, BP 220, F-38043 Grenoble Cedex, France
and ILL, BP 156, F-38042 Grenoble Cedex, France*

T. A. Pikuz and A. Ya. Faenov

Multicharged Ions Spectra Data Center of National Research Institute for Physiscal-Technical and Radiotechnical Measurements VNIIFRTI, Mendeleevo, Moscow Region 141570, Russia

(Received 25 October 2000; accepted for publication 22 April 2001)

A novel, compact, large field, and spectrally tunable imaging x-ray microscope is presented. It is based on the use of an isotropic point x-ray source and a spherically curved crystal. The x-ray beam intensity is modulated by the object attenuation, then monochromatized and enlarged using a spherical crystal and, finally, imaged using a detector downstream from the crystal. We demonstrate by ray tracing simulations that this system allows microscopy studies with high spatial resolution, high magnification ratios, and large field of view. Microscopes using this model can be easily built using different x-ray sources, like conventional x-ray tube generators, x rays emitted by laser-generated plasmas or x-pinch plasmas, and also synchrotron radiation when used in combination with other condenser optics. Preliminary experiments are presented to demonstrate the feasibility of the proposed setup. High resolution ($\sim 4 \mu\text{m}$) monochromatic ($\delta\lambda/\lambda \sim 10^{-5} - 10^{-3}$) images over a large field of view (few mm^2) were recorded in the spectral range 8–14 Å using a laser-generated plasma source and a spherical mica crystal. Compared to x-ray crystal imagers used in relation with plasma sources, the new configuration produces high quality stigmatic images working at many different Bragg angles, thus improving the spectral tunability and allowing a more flexible design. © 2001 American Institute of Physics. [DOI: 10.1063/1.1379599]

I. INTRODUCTION

X-ray microscopy produces high resolution images of objects that are opaque to other probing techniques, like optical or electronic microscopy. The domain of x-ray microscopy has seen an extraordinary development in the last decades because of three main factors: (i) availability of new sources, (ii) revolutionary developments in x-ray optics, and (iii) improvements in charge coupled device (CCD) cameras and use of new detector techniques. Different x-ray sources are used for x-ray microscopy: (i) x-ray tubes and other electron or ion impact sources, (ii) laser generated plasmas or x-pinch plasmas, and (iii) synchrotron radiation sources. Synchrotron sources are the preferred x-ray sources in terms of brightness, and presently almost every facility has one or several types of x-ray microscopy beamlines.¹ However, they require large installation and in many cases present difficult access. X-ray tubes have the advantage of being accessible in many small laboratories. A variation of the x-ray tube useful for microscopy applications can be obtained from a simple modification of an electron microscope.² Another way to create x rays is the use of a laser-produced plasma, generated by the interaction of intense pulsed (femtosecond, picosecond, or nanosecond) lasers with a solid target, or an x-pinch plasma. In such cases, the pulsed x rays are emitted isotropically from the interaction zone of dimension 5–100 μm .

Recent developments in laser technology allow compact powerful lasers designed to produce table-top x-ray sources for customized applications.

X-ray optics have presented an unprecedented development in recent years allowing submicron x-ray microprobes. Reflecting (Kirkpatrick–Baez configuration of mirrors or multilayers), refracting (compound refracting lenses), and diffracting (Fresnel zone plates, Bragg–Fresnel, and perfect crystals) systems are presently in use. Reviews on instrumentation for x-ray microscopy with photon energy below and above 1 keV are available (Refs. 3 and 4, respectively). Concerning detectors, one can now record in a very short time x-ray images with high resolution and high dynamical range thanks to improvements in CCD technology. Sophisticated three-dimensional tomographic or holographic object reconstruction is also possible. The detection of phase contrast (in addition to the standard absorption contrast) has opened new directions in x-ray microscopy. The detection of emitted fluorescence, secondary electrons, or energy-sensitive absorption has driven the creation of a new field complementary to conventional x-ray imaging microscopy: spectromicroscopy.

Two main approaches are used for x-ray microscopy: to scan the object (sample) illuminated by an x-ray microprobe, for obtaining images of the transmitted photons or fluorescence or secondary electrons (scanning microscopy); and to magnify the x-ray image itself by an optical system (imaging microscopy). The simplest way to create an imaging micro-

^{a)}Electronic mail: srio@esrf.fr

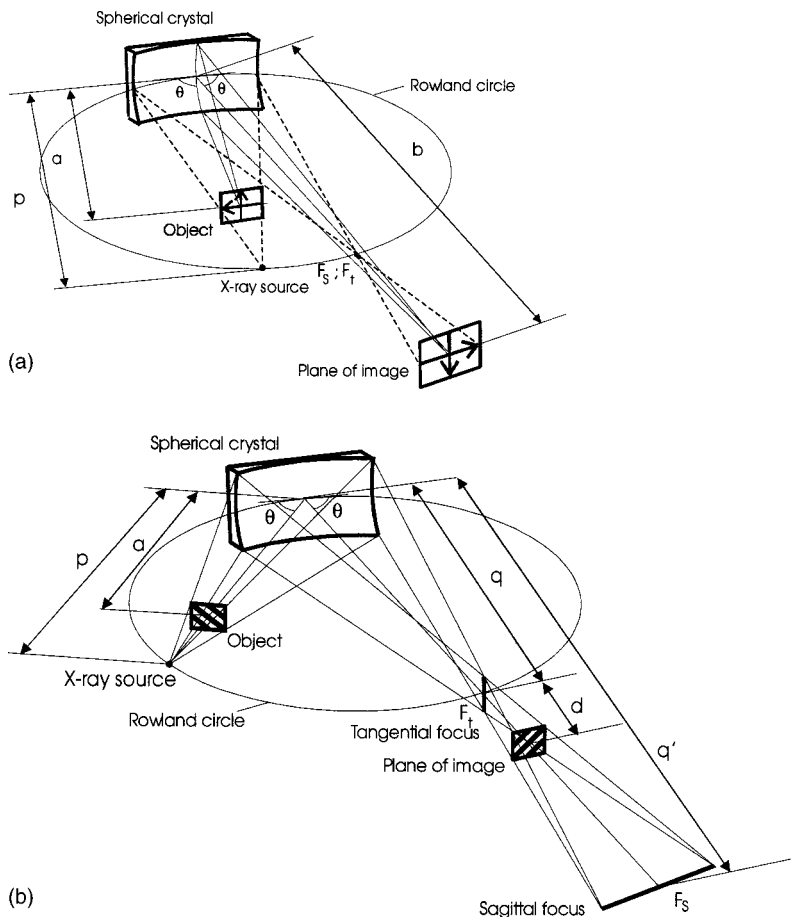


FIG. 1. Comparison between the monochromatic back-lighting scheme (top) and the novel x-ray crystal imaging microscope (XCIM) (bottom). The first one works at normal incidence and the positions of the object and image are determined by the lens equation $1/a + 1/b = 2/(R \sin \theta)$. The second one works for any Bragg angle ($\theta < 45^\circ$ is preferred, see the text) and the image plane is obtained at a distance d given by Eq. (5).

scope is to record the projected image of the object when illuminated by a point isotropic source (projection microscopy).⁵ Here, the object is placed between the source and the detector (e.g., an x-ray film). The magnification is given by the ratio of source–film to source–object distance. The transversal spatial resolution is limited by the size of the source and diffraction effects. Although this idea was realized in the 1930s, only in the 1950s was it successfully applied when x-ray tubes with well-focused electron beams ($0.1 \mu\text{m}$) were available.⁶

In this article we propose an x-ray crystal imaging microscope (XCIM). On one hand, it can be seen as a variation of the projection microscope, consisting of inserting a spherical crystal between the object and the film. Among the advantages of the XCIM with respect to the projection microscope, which is basically a microscope without optics, we can mention: (i) the monochromatization of the radiation by the crystal, improving the quality of the image, (ii) the flexibility of designing an instrument considering the fact that there are more parameters than simply the distances ratio, and (iii) the resolution depends on the source dimension, but is not limited by it (resolution is improved with respect to the projection microscope with the same magnification). On the other hand, it can be considered as an improvement of imaging crystal spectrometers in use for plasma diagnostics and applications. The surface of dense laser-produced plasmas is hot enough to produce significant quantities of x rays to be used to characterize the plasma for illuminating other objects to be imaged. In many cases, the objects are cold and dense

targets. Large magnified x-ray images have been obtained using spherically curved crystals in normal incidence,⁷ or toroidally⁸ curved crystals to relax the backscattering condition. The XCIM has many advantages compared with existing configurations. The spherical crystal is simpler to manufacture, easier to align, and can be used in a multitude of distance configurations and Bragg angles as compared to a toroidal crystal. The XCIM produces high resolution quasi-undistorted images for any Bragg angle, thus allowing a higher spectral tunability and higher field of view than conventional backscattering schemes.

The proposed microscope uses a point-like isotropic source, thus it is in principle targeted for applications using x-ray sources like x-ray tubes or point plasma x-ray sources. However, it can also be used for synchrotron radiation applications when combined with other condensing optics.

II. DESCRIPTION OF THE MICROSCOPE SETUP

The microscope system can be considered as a modification of the x-ray back-lighting system,⁷ which has been demonstrated as a successful tool in imaging laser-generated plasmas. In the traditional x-ray back-lighting scheme [see Fig. 1(a)] a spherically curved crystal (with curvature radius R) is placed on the Rowland circle of radius $R/2$. The x-ray source (backlighter) is on the Rowland circle and is imaged on another point of the Rowland circle. Placing a detector (i.e., an x-ray film or CCD camera) downstream from the focal image of the source, it is possible to obtain an enlarged

image of the source, with different magnifications depending on the distance from the focal point to the detector. If the backlighter dimensions are small (quasi-point source) and an object is placed at a distance a upstream from the crystal, then a transmission image (radiography) of the object will be observed in the detector plane at a distance b downstream from the crystal. The distances a and b are related with R and the Bragg angle θ by the lens equation

$$\frac{1}{a} + \frac{1}{b} = \frac{2}{R \sin \theta}. \quad (1)$$

The magnification of this system (in both the tangential and sagittal planes) is

$$M = \frac{b-p}{p-a}. \quad (2)$$

The magnification can be increased by either approaching the object to the source (i.e., $p-a$ tends to zero) or by moving away the detector (increasing b). It is important to note that the object can be positioned at any place between the source and the crystal, and, more importantly, the position of the detector is also free [the magnification is given by Eq. (1)]. This imaging transmission microscope only works for a limited interval of Bragg angles⁹ (80° – 90°), otherwise the aberrations (astigmatism) strongly deteriorate the image. In addition, the spectral tunability of the system is reduced because it is only possible to work at Bragg angles close to 90° , i.e., wavelengths close to multipliers of $2D$, being D the d spacing of the crystal.

One of the most important features of the proposed XCIM system [Fig. 1(b)] is the relaxation of the normal incidence condition. It can also work out of the Rowland configuration. Moreover, the detector cannot be placed at any place downstream from the focal point, as for the traditional backlighting scheme, but must be positioned at a fixed distance d from the tangential focus (see below). When considering a curved mirror or crystal with a radius of curvature R set to receive x rays from the source (placed at distance p from the center of the crystal) with a grazing (Bragg) angle θ , two focal images at distances q and q' from the crystal are formed. They correspond to the tangential and sagittal foci, respectively. The focal position q in the tangential plane is obtained from

$$1/p + 1/q = 2/(R \sin \theta) \quad (3)$$

and the focal distance q' in the sagittal plane is given by

$$1/p + 1/q' = 2 \sin \theta / R. \quad (4)$$

Formulas (3) and (4) are the extension for grazing incidence of ordinary geometric optics principles for mirrors (see, for example, Ref. 10). In the particular case of normal incidence ($\theta=90^\circ$) both foci are coincident ($q=q'$). Another important particular case that satisfies Eq. (3) is when the source, the crystal, and the tangential focal point lie on a circle of radius $R/2$, the so-called Rowland circle. The Rowland circle configuration optimizes, at the same time, the energy bandwidth of the diffracted beam and the focalization. In our case, using symmetric Bragg crystals, this condition is satisfied if $p=q=R \sin \theta$.

Let us now analyze the behavior of this system as an x-ray microscope: consider a small object in the path of the rays at a distance a upstream from the pole of the crystal and calculate the position where the ‘‘best’’ image is found. We can define the best image as the one with presents the same magnification in both the sagittal and tangential plane. Therefore the image is as ‘‘undistorted’’ as possible and presents the same aspect ratio as the imaged object. It can be easily shown that this image is found when the detector is positioned at a distance d downstream from the tangential focus:

$$d = \frac{q'q - q^2}{q' + q}. \quad (5)$$

Let us denote with Ω_i the incident divergence. Ω_r and Ω_r^{sag} are the reflected divergences in the tangential and sagittal planes, respectively. The focusing condition guarantees that $p\Omega_i = q\Omega_r = q'\Omega_r^{\text{sag}}$. The magnification in the tangential plane at the ‘‘best image’’ position can be calculated as

$$M = \frac{\Omega_r}{\Omega_i} \frac{d}{(p-a)} = \frac{p}{q} \frac{d}{(p-a)}. \quad (6)$$

With the help of Eq. (3) we obtain

$$M = \frac{d(2p - R \sin \theta)}{Rp \sin \theta(1 - a/p)}. \quad (7)$$

If we let a/p be a varying parameter, and using Eqs. (3), (4), and (5), we can express M as a function of only p , R , and the Bragg angle:

$$M = \frac{p(1 - \sin^2 \theta)}{p(1 + \sin^2 \theta) - R \sin \theta} \frac{1}{1 - a/p}. \quad (8)$$

The magnification in the M_s in the sagittal plane is

$$M_s = \frac{\Omega_r^{\text{sag}}}{\Omega_i} \frac{q' - (q+d)}{p-a} = \frac{1 - (q+d)/q'}{1 - a/p}. \quad (9)$$

Equations (6) and (9) are the general expression for the magnification in the tangential and sagittal directions, respectively. The position of the detector [i.e., best image given by Eq. (5)] does not depend on the position of the object a . However, contrary to what happens in the traditional backlighting scheme, where the detector can be positioned anywhere, the detector position depends now on the focal distances q and q' . Therefore images with different magnifications can be obtained by simply moving the object [i.e., changing a in Eq. (8)] while keeping fixed the crystal and detector.

Particular case: the source is located on the Rowland circle. In the particular case that the source, crystal, and tangential focus are placed on the Rowland circle we have

$$p = q = R \sin \theta, \quad (10)$$

therefore the magnifications takes the form

$$M = \cot^2 \theta \cdot \frac{1}{1 - a/p}, \quad (11)$$

M as a function of a/p only depends on the Bragg angle. For a given Bragg angle, M ranges from $\cot^2 \theta$ to infinity de-

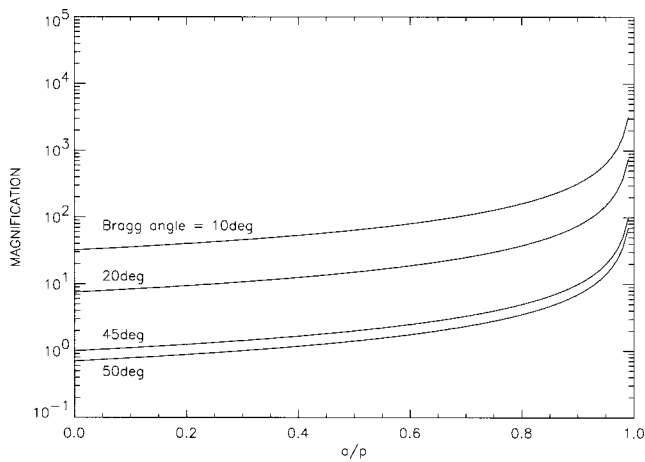


FIG. 2. Magnification vs a/p (ratio between crystal-object and crystal-source distances) for different Bragg angles.

pending on the relative distance source-object. On the other hand, if we fix a/p , then M can be made as large as wanted by decreasing the Bragg angle. This equation shows some fundamental aspects of the proposed setup: (i) one can obtain, in principle, a magnification as high as wanted, (ii) for increasing magnification one can choose between going to more grazing Bragg angles or approaching the object to the source (or a combination of both), and (iii) Bragg angles more (less) grazing than 45° will lead to a larger (smaller) magnification $M > 1$ ($M < 1$). Obviously, when M is increased (by selecting grazing Bragg angles or approaching a to p), some experimental limitations arise: for a given crystal size, the accepted divergence Ω_i is smaller when M is increased; and the field of view (or object dimension) must be smaller for a given divergence Ω_i when one approaches a to p . Figure 2 shows a plot of M versus a/p for several Bragg angles. From Fig. 2, and considering previous experimental works,¹¹ we have selected the parameters of an initial configuration that will be the “basic configuration” for our ray tracing studies. We selected $R = 15$ cm and a Bragg angle of 20° . Source and crystal are mounted in a Rowland circle configuration with $p = q = 5.13$ cm and $q + d = 43.86$ cm. When $a = 3.5$ cm, the magnification is about 24. The crystal size is about 15×50 mm². The x-ray source considered here emits isotropic radiation. We will study the effect of the source dimensions ranging from zero (point source) to several tens of microns (a typical laser generated plasma has source size of not less than $20 \mu\text{m}$).

III. RAY TRACING CALCULATIONS

The performance of a system consisting of an x-ray source and a curved crystal is analyzed using ray-tracing simulations. The x-ray source was represented by either a point source or a three-dimensional cylindrical source. In the latter case, the rays are created inside a cylinder (of several diameter and length values) whose axis is directed along the optical axis (the line between the source center and the crystal center). It is assumed that the source emits isotropically in all directions. In the simulations, for efficiency reasons, the rays are emitted into a reduced solid angle (defined by the

semiaperture of the emission cone, usually between 0.1 and 0.01 rad) which illuminates a limited area of the crystal up to the dimensions corresponding to the physical size of the available crystals (about 15×50 mm²). The crystal is placed at a distance p from the source, and is orientated to the required Bragg angle relative to the incoming beam. The crystal is considered as a “mirror-like” system, which means that each ray is reflected at the crystal surface following the laws of specular reflection (incident ray, surface’s normal and reflected ray must lie on the same plane; and reflected angle equals the incident angle). The validity of this approximation has been discussed elsewhere.¹² In a real crystal, the diffraction process takes place in a crystal volume determined by the primary extinction depth. Although this length is small for perfect crystals, it may degrade the spatial resolution of an imaging system like the one considered here. This effect limits the resolution of the microscope and is also studied by ray tracing. For that reason, mosaic crystals where the penetration of the beam inside the crystal is much larger (defined by the secondary extinction length) are less suitable for this type of microscope. Therefore, the perfection of the crystal is an important parameter to consider when designing a crystal microscope because it determines the best available resolution.

Ray tracing calculations were performed using the SHADOW package.¹³ Typical runs use 5000 rays. Several simulations have been performed to study the role of the different system parameters in the quality of the image. The goal was to obtain high magnification rates ($M > 10$) with spatial resolution of the order of microns, when using x-ray sources with dimensions of several microns and spherically bent crystals with radii in the interval 8 – 20 cm. We show how the quality of the image (uniformity of magnification and spatial resolution) is influenced by experimental parameters like geometrical errors of the crystal figures (uniformity of the curvature radius), crystal size or entrance pupil, source depth and size, and grazing Bragg angle. The results of this study can then be used to design a suitable XCIM to match the user requirements.

IV. RAY TRACING RESULTS

A. Results for the basic configuration

Several ray tracing experiments have been performed to confirm the validity of formulas (5)–(11). A source that emits “rays” randomly distributed in a cone of semiaperture either 0.01 or 0.1 rad has been used. It emits isotropic radiation and has dimensions of either zero (point source) or $20 \mu\text{m}$. The crystal parameters are $R = 15$ cm and $\theta = 20^\circ$. The source and crystal are located on the Rowland circle with $p = q = 5.13$ cm. The best image position is found at $q + d = 43.86$ cm ($d = 38.72$ cm). When $a = 3.5$ cm, the magnification is $M = 23.76$.

In Fig. 3 we can see the calculated image produced by an absorbing mesh grid of $120 \mu\text{m}$ period and $14 \mu\text{m}$ thickness imaged at the object position and at the detector position. Two images are presented: the mesh grid (object) plane and the detector (image) plane. A first run has been done using a beam divergence of 0.01 rad. A $20 \mu\text{m}$ diameter source with

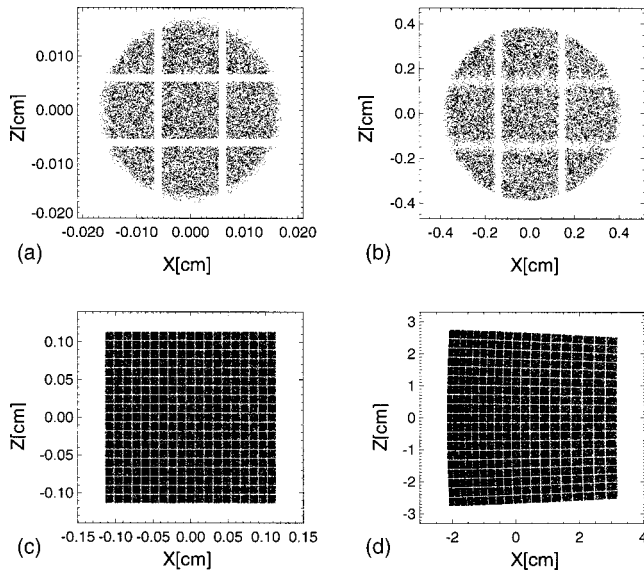


FIG. 3. Ray tracing results for the basic configuration: $R=15$ cm; source located on the Rowland circle: $p=q=5.13$ cm; $q+d=43.86$ cm; $a=3.5$ cm, and $M=24$. The grid period and thickness are 120 and $14 \mu\text{m}$, respectively. (a) and (c) represent the grid (object plane), whereas (b) and (d) show the image of the grid in the image plane. Note that the scale of the images (right graphs) is different from the object's one (left), showing a magnification of about $M=24$. The top figures [(a) and (b)] are calculated using a cylindrical source of $20 \mu\text{m}$ diameter and 1 mm height, which emits randomly in a cone of semiaperture 0.01 rad. Bottom: The bottom figures [(c) and (d)] are calculated using a source with no dimensions (point source) with a divergence (semiaperture) of 0.1 rad.

a height of 1 mm has been used. The image at the detector plane [Fig. 3(b)] shows some important facts: (i) the $14 \mu\text{m}$ thick wires are perfectly visible (demonstrating high spatial resolution, better than the source size), (ii) the image presents the same aspect ratio in tangential (diffraction) and sagittal planes, and (iii) the spatial resolution is better in the tangential plane (horizontal direction in the figure) than in the sagittal one (vertical in the figure). The latter effect is explained in the Appendix. We want to emphasize that these results are obtained for a Bragg angle ($\theta=20^\circ$) far from backscattering, and are confirmed by experimental tests (see below).

In the traditional backlighting scheme, for a given crystal setup (i.e., fixing p , R , and θ) there is an infinity of pairs of values (a, b) that gives the same magnification M . It is well known that this scheme works well for imaging applications in normal incidence. In the case of non-normal incidence, there is, however, only one pair of values (a, b) that produces an image with the same aspect ratio as the object, and this is the one that corresponds to the XCIM case. In other words, the XCIM setup is the same as the traditional backlighting scheme, but the degeneration in the solution for (a, b) is broken to fulfill the condition of identical aspect ratio for the image and object. A second SHADOW run has been done using a point source of divergence 0.1 rad. In this case, the size of the illuminated object (field of view) is 3 mm, and the footprint on the crystal (tangential direction) is 15 mm. The result [Fig. 3(d)] still shows a high resolution image, but with an appreciable distortion in regions far from the center.

B. Change in magnification due to object thickness or object displacement

In a real experiment, the object to be imaged is not a plane but a volume, thus it has a given thickness in the beam direction. In consequence, if we consider the object to be composed by a collection of thin slices in the beam direction, each slice will be positioned in a different object plane (i.e., different a value) and then each slice will be affected by a different magnification M . This implies an aberrated image due to the fact that parts of the object closer to the source are more magnified than the parts further from the source. An equivalent effect is obtained when displacing a plane object in the direction parallel to the beam.

Let us study how M changes with respect to its mean value as a function of a small change of the parameter a . Calling Δa the thickness and/or the error on the object position, we can calculate its effect on magnification and then check it with ray tracing. When θ and p are kept fixed, the change in magnification due to Δa is

$$\Delta M = \left(\frac{\partial M}{\partial a} \right)_{p, \theta} \Delta a, \tag{12}$$

therefore

$$(\Delta M/M)_{p, \theta} = \Delta a / (p - a). \tag{13}$$

If we think in different experimental configurations defined by pairs (R, θ) which give the same M , then the most critical configurations are those for which $(p - a)$ is small. For a given R , $(\Delta M/M)_{p, \theta}$ is larger at high Bragg angles because in this case one has to put $a/p \rightarrow 1$ in order to obtain the wanted magnification M . $(\Delta M/M)_{p, \theta}$ also increases when decreasing R if both θ and a/p are fixed. Table I shows the results of both ray tracing and analytical calculations for three pairs (R, θ) which give approximately the same magnification ($M \sim 24$). A value of $\Delta a = 1$ mm has been considered. When both θ and a/p are fixed, then $(\Delta M/M)_{p, \theta} \propto \Delta a / R$; when, instead, we increase θ , we have to make a/p closer to 1 in order to get the same M , and then the relative change in magnification increases. From these results we can conclude that the XCIM is not very sensitive to the object thickness or displacements, thus making it suitable for imaging three-dimensional objects.

C. Change in magnification due to uncertainty on the radius of curvature or Bragg angle

When R and/or θ change the variations of M have to be calculated after considering the following: (i) we are no longer in the Rowland circle, so the general expression for M has to be considered; (ii) such a expression is not the same for the tangential and sagittal directions; (iii) the image we look at is no longer the best image; our image is located at a distance d from the tangential focus that is given by $d = d_0 + \Delta d$ with d_0 the distance for the unperturbed system given by Eq. (5), and $\Delta d = -\Delta q = q_0 - q$, the difference between the distances to the tangential focus for the unperturbed and perturbed systems; and (iv) the factor $1/(1 - a/p)$ remains unchanged.

TABLE I. Change in magnification due to object thickness or position error Δa . The magnification values are calculated exactly, and relative variations of M calculated by Eq. (13) are compared with values obtained by ray tracing.

Theta (deg)	Radius (cm)	p (cm)	a (cm)	Δa (cm)	Relative variation of M				
					Magnification		Ray tracing		
					Sagittal	Tangential	Sagittal	Tangential	Calculated
20	15	5.13	3.5	0	23.7	23.7			
		5.13	3.4	-0.1	22.4	22.2	-5.4%	-6.3%	-6.0%
		5.13	3.6	0.1	25.3	25.4	6.6%	6.9%	6.3%
20	25	8.55	5.85	0	24.0	24.0			
		8.55	5.75	-0.1	23.3	23.1	-3.0%	-3.6%	-3.6%
		8.55	5.95	0.1	24.9	24.7	3.6%	3.0%	3.8%
45	25	17.68	16.94	0	24.0	24.0			
		17.68	16.84	-0.1	20.4	20.6	-14.9%	-14.3%	-12.7%
		17.68	17.04	0.1	27.9	27.9	16.1%	16.1%	14.5%

Equations (6) and (9) give the magnification in the tangential and sagittal directions, respectively. When R and/or θ change we have

$$(\Delta M/M)_{a,p}^{\text{sag}} = \frac{\Delta q'}{q'} \left(\frac{d_0 + q_0}{q'_0 - q_0 - d_0} \right), \quad (14)$$

$$(\Delta M/M)_{a,p}^{\text{tan}} = -\frac{\Delta q}{q} \left(\frac{d_0 + q_0}{d_0 - \Delta q} \right) \quad (15)$$

for the sagittal and tangential planes, respectively. For the basic configuration, $q_0, q'_0 \ll d_0$, then

$$(\Delta M/M)_{a,p}^{\text{sag}} = -(\Delta q'/q')_{a,p}, \quad (16)$$

$$(\Delta M/M)_{a,p}^{\text{tan}} = -(\Delta q/q)_{a,p}. \quad (17)$$

From Eqs. (16) and (17) one obtains the change in M in the sagittal and tangential planes, respectively, related to the change in R :

$$(\Delta M/M)_{a,p,\theta}^{\text{sag}} = (\Delta R/R)/[1 - R/(2p_0 \sin \theta)], \quad (18)$$

$$(\Delta M/M)_{a,p,\theta}^{\text{tan}} = -(\Delta R/R)/[1 - (R/2p_0) \sin \theta]. \quad (19)$$

In a similar way, the change of magnification with respect to variations in the Bragg angle is

$$(\Delta M/M)_{a,p,R}^{\text{sag}} = \frac{\cot \theta}{1 - R/(2p_0 \sin \theta)} \Delta \theta, \quad (20)$$

$$(\Delta M/M)_{a,p,R}^{\text{tan}} = -\frac{\cot \theta}{1 - (R/2p_0) \sin \theta} \Delta \theta. \quad (21)$$

Comparisons between calculated values using these formulas with ray tracing results are shown in Table II. These results verify the stability of the XCIM versus small errors in crystal curvature and Bragg angle.

D. Distortion of the image

We have seen that a distortion of the image appears when the accepted source divergence is large. From Fig. 3(a) one can see that the image using a 0.01 rad divergent source is mainly undistorted, whereas for a source ten times more divergent [Fig. 3(b)] the image is slightly distorted, but conserving a good spatial resolution. This means that magnification at the image edges is different than the one at the center of the image. In order to study this effect, we have created a point source with divergence in a grid scale from 0 to 0.1 rad. The source projection at the object plane for the basic configuration is in Fig. 4 (top left). The magnified image is also in Fig. 4 (top right). A deformation in the tangen-

TABLE II. Change in magnification due to errors in radius of curvature (a) and Bragg angle (b). The magnification values are calculated exactly, and the relative variations of M calculated by Eqs. (18) and (19) in (a) and by Eqs. (20) and (21) in (b) are compared with values obtained by ray tracing.

(a)				Relative variation of M					
Theta (deg)	Radius (cm)	$p_0 = q_0$ (cm)	ΔR (cm)	Magnification		Ray tracing		Calculated	
				Sagittal	Tangential	Sagittal	Tangential	Sagittal	Tangential
20	15	5.13	0	23.7	23.7				
		5.13	0.5	24.0	22.1	1.0%	-6.9%	1.0%	-6.7%
		5.13	-0.5	23.6	25.7	-0.6%	8.4%	-1.1%	6.7%
(b)				Relative variation of M					
Theta (deg)	Radius (cm)	$p_0 = q_0$ (cm)	$\Delta \theta$ (cm)	Magnification		Ray tracing		Calculated	
				Sagittal	Tangential	Sagittal	Tangential	Sagittal	Tangential
20	15	5.13	0	23.7	23.7				
		5.13	0.1	23.7	23.4	0.0%	-1.5%	-0.15%	-0.96%
		5.13	-0.1	23.7	23.9	0.0%	0.9%	0.15%	0.96%

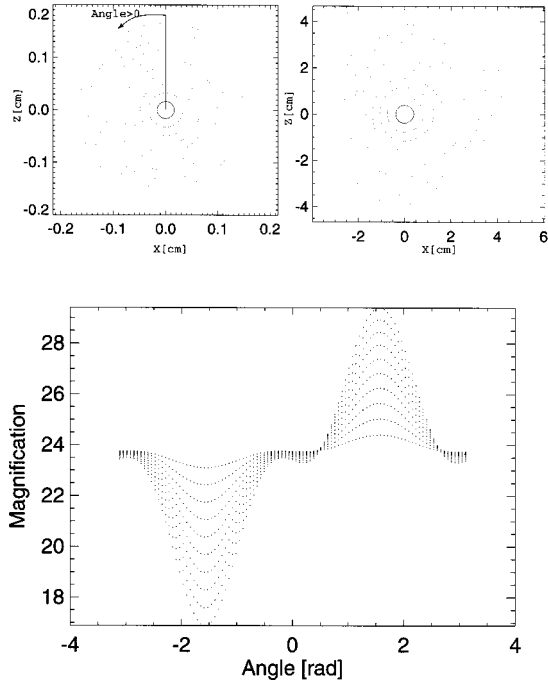


FIG. 4. Top: Grid source imaged in the object plane (left) and in the image plane (right). Units are in cm. Bottom: The magnification for the different points in the top figure as a function of the polar angle. The origin and positive direction of the polar angle are indicated with a vertical line and an arrow, respectively, in the top-left figure.

tial plane (horizontal in the graph) is clearly seen when the source divergence is increased. Giving a point in the image (a given ray), we can calculate the ‘‘local’’ magnification for that point by calculating the ratio between the distance to the center of the image plane in such an image over the same magnitude in the object plane. That means

$$M_i = \frac{\sqrt{X_i^2 + Y_i^2}}{\sqrt{x_i^2 + y_i^2}}, \tag{22}$$

where (X_i, Y_i) are the coordinates of the i th ray in the image plane, and (x_i, y_i) are the coordinates in the object plane. The plot of magnification as a function of the polar angle (Fig. 4, bottom) clearly shows the error in magnification for the different circles corresponding to different source divergences. This error is maximized at the angles $\pm \pi/2$ (see Fig. 4, bottom) corresponding to the points more distant from the optical axis in the tangential direction. Clearly, this distortion effect should disappear if the rays reflected by the crystal surface would satisfy the Abbé sine condition.¹⁴ This law must be verified (at least approximately) by any optical sys-

tem to form an undistorted image. In grazing incident systems, the magnification for rays coming from a point source that arrive at different positions on the reflecting surface is, in general, different. It can be easily demonstrated that the sine condition cannot be satisfied if only a single reflecting surface is used. One could think that distortion can be reduced by a small rotation of the detector plane around a vertical axis. Some simulations were done to verify this hypothesis without success: in the best case it is sometimes possible to improve an edge of the image but additional distortions appear in the rest of the image. Other simulations were done using an ellipsoidal crystal. The resulting distortions have similar magnitude than those produced by spherical crystals. In conclusion, an ellipsoidal crystal, which eliminates the spherical aberrations in the point-to-point focusing, does not improve the quality of the image because it does not fulfill the Abbé sine condition.

E. Depth of focus

The depth of focus, or more precisely, the allowed detector displacement (errors in d) without significant change in magnification, is very large for the XCIM. Some calculations demonstrate that one can safely move the position of d by several mm without significant distortion of the image. The relation between the magnification and the distance d is linear [Eqs. (16) and (17)]. Therefore the relative change in magnification due to a displacement Δd of the image is given by

$$(\Delta M/M)_{a,p,R,\theta}^{\text{sag}} = -\Delta d / (q' - q - d), \tag{23}$$

$$(\Delta M/M)_{a,p,R,\theta}^{\text{tan}} = \Delta d / d. \tag{24}$$

The results of the ray tracing compared with those calculated using these formulas are in Table III. This small sensitivity of the magnification to even large changes in detector position is important for practical applications.

F. Spatial resolution versus source dimension

It is essential to have an idea of the achievable resolution when a real source (i.e., an extended source) is used. It is possible to evaluate visually the resulting images of the ray tracing (e.g., Fig. 3) and then assess the spatial resolution. As an example, from Fig. 3 we can say that there is a very good resolution in the tangential plane, a worse resolution in the sagittal one, and in both cases the resolution is better than $14 \mu\text{m}$, because the grid wires of this dimension are well resolved. Simple geometrical arguments (see the Appendix)

TABLE III. Influence of the errors in detector position on the magnification. The magnification values are calculated exactly, and the relative variations of M calculated by Eqs. (23) and (24) are compared with values obtained by ray tracing.

Theta (deg)	Radius (cm)	$p = q$ (cm)	q' (cm)	Δd (cm)	Relative variation of M					
					Magnification		Ray tracing		Calculated	
					Sagittal	Tangential	Sagittal	Tangential	Sagittal	Tangential
20	15	5.13	-6.7	0	23.7	23.7				
				0.5	23.9	24.1	0.9%	1.8%	1.0%	1.3%
				-0.5	23.4	23.4	-1.2%	-1.5%	-1.0%	-1.3%

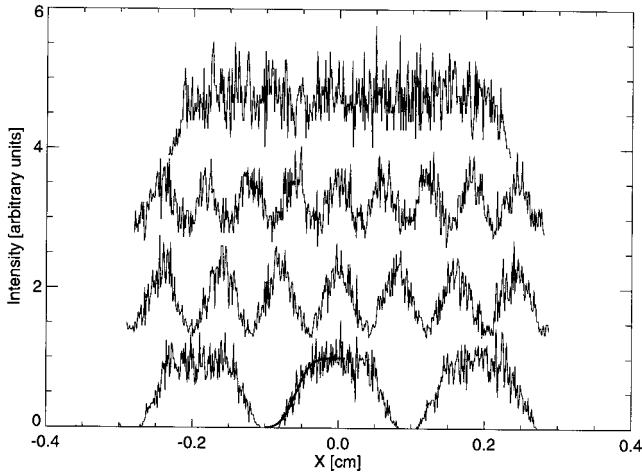


FIG. 5. From bottom to top: (1) resolution histogram at the image plane using a $20\ \mu\text{m}$ source when imaging a grid of $f=30\ \mu\text{m}$ feature and $80\ \mu\text{m}$ periodicity. The overplotted thick line is the error function fit of the edge from where the resolution value of $r=17\ \mu\text{m}$ is obtained. (2) image with the same source produced by a grid with feature $f=r$ and period $2f$. (3) Same as (2) but for $f=0.75r$. (3) Same as (2) but for $f=0.5r$.

show that the spatial resolution of the XCIM is, in general, better than the projection microscope with the same magnification. Moreover, the XCIM resolution is better in the tangential (diffraction) plane than in the sagittal one.

It is convenient to define a method to obtain quantitative value of the spatial resolution from the image scattered plots. For that, histograms of the ray distribution on the “best image” plane are computed in both tangential and sagittal directions. The image of an edge in the object produces some slope in the histogram. From that slope it is possible to determine a value of the spatial resolution. We have fitted the histogram edges to an error function $\text{erf}(x) = a \int_{-\infty}^x e^{-[(x-x_0)/\sigma]^2}$ in order to determine this value. The σ value resulting from the fit gives the resolution value $r=2\sigma/M$, with M the magnification. This resolution value means that for a grid of feature f and period $2f$, then if $f=r$ the grid is completely resolved in the image plane (if $f=0.5r$ the grid is not resolved at all; and if $f=0.75r$ the grid is semiresolved). An example to illustrate this fact is reported in Fig. 5. For obtaining good quality histograms (acceptable noise with a small bin step) 50 000 rays were used in SHADOW runs. In Table IV the results of this procedure for different source size are reported. Calculations were done by adjusting the grid feature in order to obtain a histogram with intensity zero in the obscured part. It is possible to clearly resolve features of less than $10\ \mu\text{m}$ in the object using a magnification of $M=24$ and with a source diameter up to about of $20\ \mu\text{m}$. The source depth can be as large as 1 to 2 mm.

The results reported in Table IV show that similar values of resolution as obtained for $R=15\ \text{cm}$ can also be obtained for $R=8$ and $25\ \text{cm}$ ($\theta=20^\circ$ in both cases). The resolution of the images using a point source is always zero. When the source is not a point, we obtained similar values of the resolution for different R values at $\theta=20^\circ$. The resolution is worse at a Bragg angle of 40° than of 20° when an extended source is used. This effect is due to the fact that when the

TABLE IV. Resolution values for different values of θ , R , and source size. The magnification, in all cases, is around $M=23.5$.

System	Source diameter (μm)	Tangential (μm)	Sagittal (μm)
$\theta=20^\circ$ $R=8\ \text{cm}$	20	4.8	16.2
	$p=2.74\ \text{cm}$ $a=1.86\ \text{cm}$	40	9.9
$\theta=20^\circ$ $R=15\ \text{cm}$	20	4.8	17.0
	$p=5.13\ \text{cm}$ $a=3.5\ \text{cm}$	40	9.1
$\theta=20^\circ$ $R=25\ \text{cm}$	20	5.3	15.9
	$p=8.55\ \text{cm}$ $a=5.85\ \text{cm}$	40	10.0
$\theta=20^\circ$ $R=100\ \text{cm}$	20	5.2	11.8
	$p=34.2\ \text{cm}$ $a=23.2\ \text{cm}$	40	10.1
$\theta=40^\circ$ $R=25\ \text{cm}$	20	12.9	15.8
	$p=16.1\ \text{cm}$ $a=15.5\ \text{cm}$	40	25.2

Bragg angle is increased the object has to be closer to the source in order to obtain the same magnification. Thus the effect of the size of the source is more significant for less grazing Bragg angles. However, for all considered cases, spatial resolution values smaller than the size of the source are obtained.

G. Effect of the crystal extinction length in the spatial resolution

In a real crystal, the diffraction effect takes place in a finite volume inside the crystal, and not on the crystal surface. This creates aberrations in the wave front after diffraction by the crystal. Therefore a degradation of the in spatial resolution of the XCIM is expected. The beam penetrated into the crystal to a depth that depends on the extinction length, which is given by the dynamical theory of diffraction. When the crystal is perfect, only the primary extinction is responsible for the penetration. Primary extinction length is of the order of a few microns (e.g., 18 and $15\ \mu\text{m}$ for Si (111) and (220) at 8 keV, respectively, and 32, 28, and $38\ \mu\text{m}$ for mica (004), (006), and (008), respectively, also at 8 keV). The penetration depth is increased when the crystal imperfection are larger. For mosaic crystals (ideal imperfect crystals) the effect of the secondary extinction increases the penetration length up to few mm. The penetration effect determines the limiting resolution of the XCIM. In order study it we have modified SHADOW to allow rays to travel inside the crystal a given distance Λ . Let us call Λ_e the mean penetration length, corresponding to the primary extinction length for perfect crystals. It is measured in the direction of the incident ray. A perfect monochromatic collimated beam will penetrate inside the crystal, losing intensity as far as diffracted photons will come in. The probability of a photon to be reflected (i.e., diffracted) after having traveled a length Λ inside the crystal is

$$p(\Lambda) = \frac{e^{-(\Lambda/\Lambda_e)}}{\int_0^\infty e^{-(x/\Lambda_e)} dx}. \quad (25)$$

We calculate the penetration Λ for each ray by Monte Carlo sampling the probability distribution given by Eq. (25). The

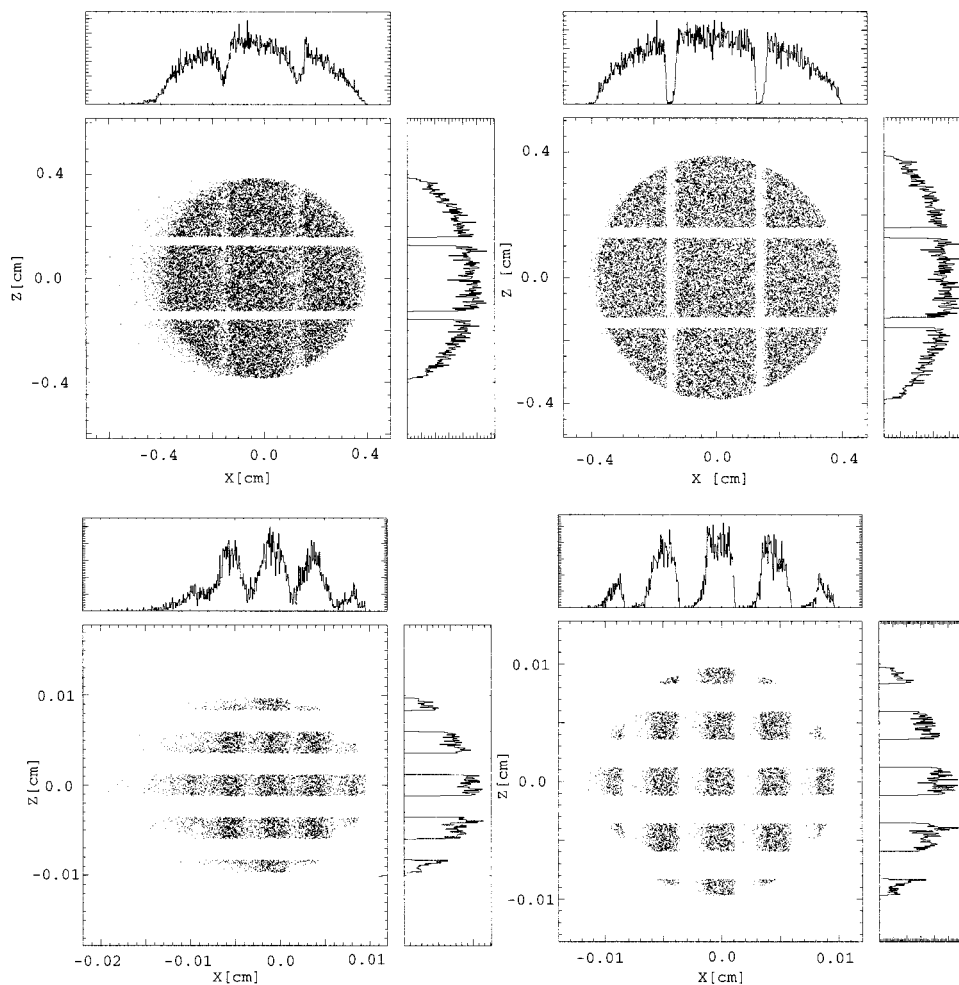


FIG. 6. Effect of the penetration length in the crystal. Top: Image of a grid of $120\ \mu\text{m}$ periodicity and $14\ \mu\text{m}$ wire thickness using the basic configuration. The penetration length is $500\ \mu\text{m}$ (left) and $100\ \mu\text{m}$ (right). Bottom: Image of a grid of $2\ \mu\text{m}$ periodicity and $1\ \mu\text{m}$ wire thickness using the basic configuration. The penetration length is $25\ \mu\text{m}$ (left) and $5\ \mu\text{m}$ (right). We observe that resolutions of about $10\ \mu\text{m}$ can be obtained with penetration depths of a few hundreds of μm and submicron resolution is possible with penetration depth of a few μm .

reflected ray direction is calculated by using the specular reflection laws considering the normal to the crystal at the intercept point.

We have performed several runs for the basic configuration with different values of Λ_e . Results show that Λ_e less than $100\ \mu\text{m}$ does not alter significantly the quality of the image [see Fig. 6(a)]. This result suggested the question of whether it could be possible to obtain submicron resolution using a XCIM. To demonstrate this hypothesis, using the basic configuration with a point source, we have imaged a grid with $2\ \mu\text{m}$ period and $1\ \mu\text{m}$ wire thickness. The magnified image of such a grid [Fig. 6(b)], is computed using Λ_e values of 5 and $25\ \mu\text{m}$ (the order of the primary extinction length for perfect crystals like Si or Ge). From these images it is evident that the $1\ \mu\text{m}$ features of the grid are perfectly resolved. Note that the penetration depth creates an asymmetry in the wire profile: it deforms one edge more than the opposite one.

V. APPLICATIONS

A. Preliminary experimental results

Preliminary test measurements demonstrate experimentally some characteristics of the proposed XCIM mentioned above. The x-ray source was a plasma created by the interaction of $10\ \text{ns}$ XeCl excimer laser pulses with energy about $1.5\ \text{J}$ with a solid target.¹¹ By selecting the right target ma-

terial and choosing the appropriate laser intensity one can vary the spectrum of the emitted x rays. We used a Ni+Cr target to obtain radiation in the neighborhood of $\lambda = 12.65\ \text{\AA}$. The size of the plasma spot emitting x ray was about $20\text{--}40\ \mu\text{m}$. The (002) reflection of a spherically curved ($R = 8\ \text{cm}$) mica crystal ($2D \sim 19.9\ \text{\AA}$) of dimensions $10 \times 30\ \text{mm}^2$ was used. Figure 7 shows a monochromatic image of a double grid obtained with a Bragg angle of $\theta = 39.4^\circ$ ($\lambda = 12.65\ \text{\AA}$). A very sharp image with high resolution (about $3\ \mu\text{m}$) for the whole field of view ($1.2 \times 2\ \text{mm}^2$) was obtained. Moreover, from the image of a single wire ($14\ \mu\text{m}$ thick), it can also be appreciated that the spatial resolution is slightly different for the horizontal (tangential plane, the size of the imaged wire is $15\ \mu\text{m}$) and vertical (sagittal plane, with a size of $18\ \mu\text{m}$) directions. Results of ray tracing simulations for this configuration gave resolution values (obtained from the image histograms, as explained before) of 3.6 and $17.5\ \mu\text{m}$ for the tangential and sagittal directions, respectively, using a $20\ \mu\text{m}$ source. If a $40\ \mu\text{m}$ source is used instead, the corresponding calculated values are 6.3 and $40\ \mu\text{m}$.

In order to test the ability to image three-dimensional (3D) objects (i.e., objects with a finite thickness) like a plasma, a structured object, or a biological sample, we placed two separated grids (with a wire thickness of $10\ \mu\text{m}$ and period of $50\ \mu\text{m}$) mounted at a distance of $2.5\ \text{mm}$, and rotated 45° with respect to the other. The image (Fig. 8)

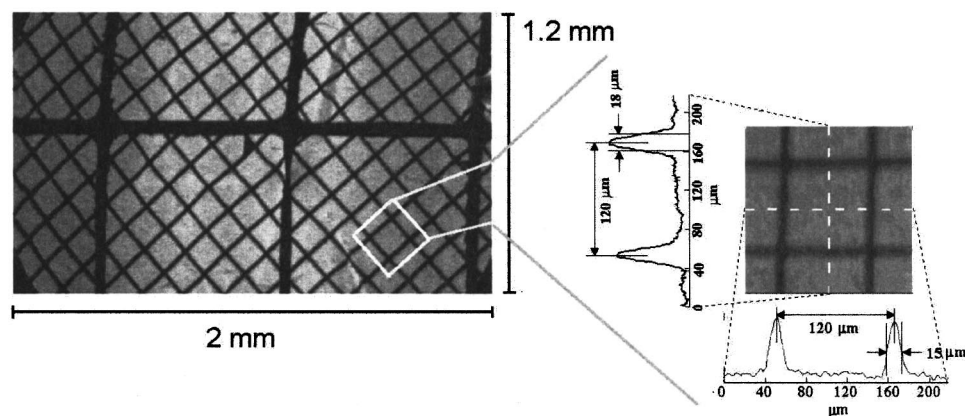


FIG. 7. Monochromatic image (from Ref. 11) of a double grid (thin grid: wire thickness $14\ \mu\text{m}$, period $120\ \mu\text{m}$; thick grid: wire thickness $60\ \mu\text{m}$, period $760\ \mu\text{m}$) at $\lambda = 12.65\ \text{\AA}$ ($\theta = 39.4^\circ$) with magnification $M = 5$ ($p = 5.08\ \text{cm}$, $a = 3.58\ \text{cm}$, $d = 7.53\ \text{cm}$), and densitogram of a part of the image. A XeCl laser with a pulse energy of $1.3\ \text{J}$ and duration of $10\ \text{ns}$ was used to create a plasma on a Ni+Cr target. A mica crystal with a radius of curvature $R = 8\ \text{cm}$ was used in first order of reflection.

obtained with $\theta \sim 45^\circ$ ($\lambda \sim 14.1\ \text{\AA}$) clearly resolves simultaneously both grids with a spatial resolution of about 3 to $4\ \mu\text{m}$ at the whole field of view. In order to illustrate this important feature, an image of a mosquito (real example of a 3D nonhomogeneous object) was obtained under the same experimental conditions, shown in Fig. 9. We should emphasize that the source size is never smaller than $20\ \mu\text{m}$, thus demonstrating the ability of the XCIM to resolve features with dimensions smaller than the source size, and with a quality of the image better than the projection microscopy with the same magnification, as predicted by ray tracing simulations.

B. X-ray sources for the XCIM

The microscope proposed here has immediate applications when used with a small and divergent x-ray source. These characteristics are presented by x-ray tubes and laser generated plasmas. The important parameter is the source size, which may be too large in conventional x-ray tubes. X-ray tubes with microfocused electrons are commercially available. The x-ray source size (electron beam focus in the target) can be set down to around $1\ \mu\text{m}$ diameter.

Laser generated plasmas and x pinches are good candidates for being used as bright x-ray sources. Laser plasma produce pulsed radiation at wavelengths down to around $1\ \text{nm}$ using a commercially available laser, which can be available in small and medium size laboratories. They could also generate much shorter radiation if tera-watt laser pulses are

employed.¹⁵ The typical sizes of laser-generated plasmas are of the order of tens of microns. Our test experiments were done with x rays with wavelengths of $12\text{--}15\ \text{\AA}$ produced by laser-generated plasmas.

The excellent properties of the synchrotron radiation allowed building the best performing x-ray microscopes available at present. Therefore it would be desirable to use the XCIM in a synchrotron radiation beamline. However, synchrotron radiation is, by nature, very collimated and with a small cross section, therefore not suitable directly for the proposed microscope. It is necessary to use additional optics to prepare the x-ray beam into a point divergent virtual source for the microscope. Synchrotron radiation condensers for undulator beamlines in low emittance storage rings are thoroughly examined by Niemann.¹⁶ Fresnel zone plates (FZP) can be used to strongly demagnify the synchrotron source, thus creating a secondary almost point source with a larger divergence, and then place the crystal microscope. The present technology allows manufacturing FZP for extreme uv, soft x rays¹⁷ and even for hard x rays applications.¹⁸ For creating a divergent beam, a FZP with a short focal distance (e.g., $10\ \text{cm}$), and a larger diameter (larger than $200\ \mu\text{m}$) is required. These values produce beams with divergencies sufficient to illuminate an object of tens of microns placed several cm downstream from the virtual size. Other ways to prepare a quasi-point divergent source using cylindrical or elliptical Kirkpatrick–Baez systems (with mirrors, multilayers, or crystals) may also be used. With synchrotron radia-

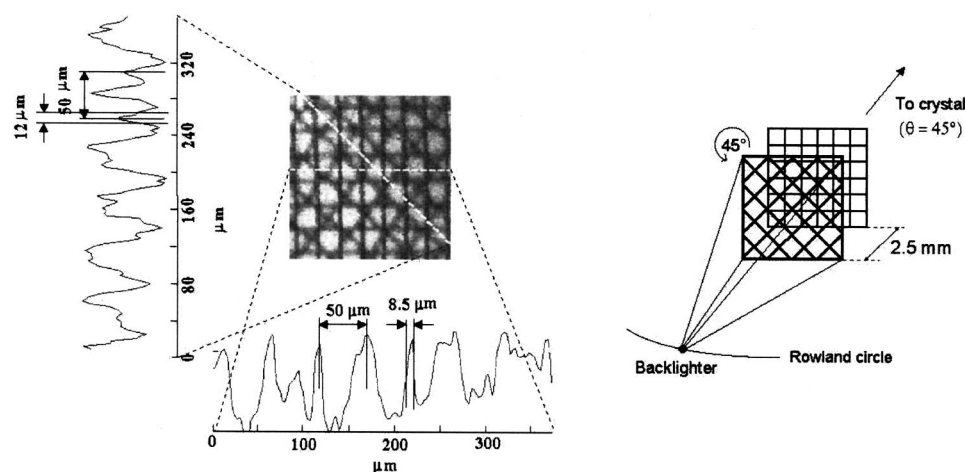


FIG. 8. Monochromatic image (from Ref. 11) of two small grids with a wire thickness of $10\ \mu\text{m}$ and period of $65\ \mu\text{m}$ at the wavelength $14.1\ \text{\AA}$ with magnification M about 4 ($p = 5.66\ \text{cm}$, $a = 4.36\ \text{cm}$, $d = 4.54\ \text{cm}$) and densitograms of the image. The grids were separated $2.5\ \text{mm}$ along the source–crystal direction and rotated by 45° one respect to the other.

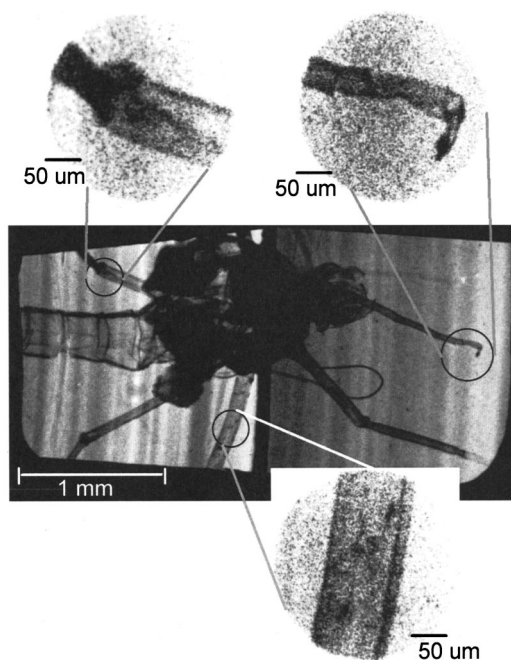


FIG. 9. Monochromatic image (from Ref. 11) of a mosquito, obtained under the same experimental conditions as Fig. 8.

tion, this previous optics allows one, *per se*, to produce an image of the object without the need of an XCIM. Thus the use of an XCIM is only interesting if other additional benefits are considered, like an improvement of the quality of the image, or further monochromatization of the beam.

C. Techniques and applications

The possible applications of the XCIM are those of the imaging x-ray microscopes: biology, chemistry, metallurgic, etc. An extended description is out of the scope of this article.

The energy range of applicability of the XCIM is that of the sources and crystals available. In addition to the crystal perfection, it is also very important to curve it to the correct spherical shape without important distortions.

The microscope presented here can be used for applications that require x-ray imaging microscopy from energies below 1 keV up to several tens of keV. Synthetic perfect crystals like Ge and Si can be used for energies larger than 3 to 4 keV. Less perfect natural crystals, like mica and quartz, are used successfully down to energies of 0.6 and 1.5 keV, respectively. The optical setup of the XCIM could, in principle, work for soft x rays using mirrors with multilayer coating instead of crystals. The energy range of the water window (2.3–4.3 nm) may be accessible using adequate multilayers or mirror coating. The larger penetration of the beam inside the mirrors should be considered, and *ad hoc* ray tracing simulations could be needed.

The XCIM can be tuned to work in different wavelengths by selecting the appropriated Bragg angle and harmonic. By adjusting the XCIM parameters it is possible to use unique crystals for several configurations (magnification, wavelength, etc.). The XCIM can be used for microspectroscopic studies [micro-extended x-ray absorption fine struc-

ture (EXAFS) and x-ray absorption near-edge structure (XANES)]. If a white or pink x-ray source is available, it is possible to scan θ in such a way that it produces an energy scan of about 100 eV (XANES) or 1000 eV (EXAFS) while the object and detector are unchanged. If the energy scan is selected around the absorption edge of one element present in the sample, then it is possible to discriminate from the object zones of a different chemical environment or electronic structure (information provided by XANES) or local structure around the absorber element (EXAFS and XANES). From Eq. (7) there is a different magnification of the image for different scanning angles. This deformation may be neglected in some cases or could be corrected in the data analysis process.

X-ray imaging microscopes, including the XCIM, can be used for microtomographic reconstruction of three-dimensional objects.¹⁹ Here, a series of images must be recorded while the object is rotated. A computer reconstruction will create 3D maps from the individual images.

The XCIM would also allow for phase contrast detection, depending on the coherence quality of the x-ray beam, nature of the object sample, and distances between elements. It has been shown²⁰ that the diffraction by a crystal in reflection mode with atomic planes parallel to the crystal surface (symmetric Bragg reflection, like the one used for the XCIM) does not alter the coherence of the beam. Finally, the XCIM can also be used for imaging applications with the purpose to obtain demagnified (instead of enlarged) images of objects.

In summary, we proposed to use a single spherically curved crystal to produce magnified images of 3D objects using a point-like x-ray source. The main characteristics of this microscope are large field of view, high resolution, spectral tunability, and simple and compact design. The parameters governing such a new schema, as well as the performances and limitations, have been thoroughly analyzed in the text using simple analytical formulas and ray-tracing simulations. Preliminary experiments confirmed the predictions.

ACKNOWLEDGMENTS

The authors would like to thank F. Flora, S. Bollanti, P. Di Lazzaro, T. Letardi, and A. Reale from ENEA-Frascati (Italy), and A. Zigler and M. Fraenkel from Hebrew University of Jerusalem (Israel) for helpful discussions and access to their laser installations. The authors are also in debt to R. Felici for fruitful discussions, and E. Di Fabrizio and F. Romanato for helpful advice on Fresnel zone plates.

APPENDIX: MAGNIFICATION OF THE SOURCE IN THE TANGENTIAL AND SAGITTAL PLANES

One may explain the improved resolution of the XCIM, when compared to the projection microscope, by considering some geometrical facts of the image formation. The intensity distribution of the image can be estimated as a convolution of the ideal magnified image with a function that takes into account the source dimension.

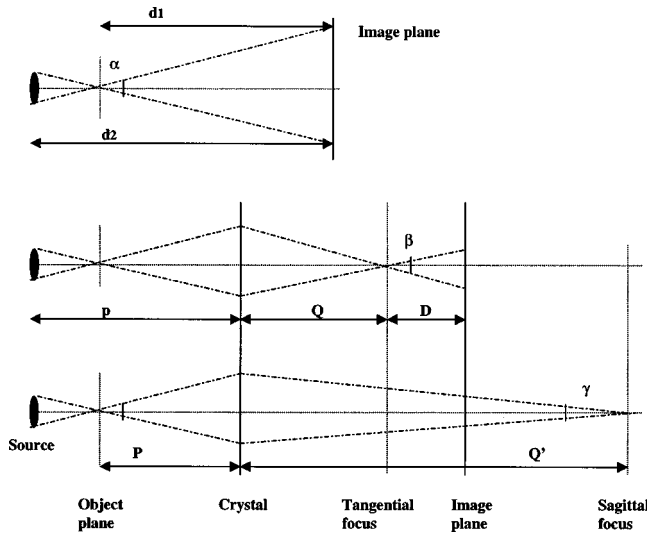


FIG. 10. Top: Schematic view of the source magnification of the projection microscope. Bottom: Schematic view of the source magnification of the XCIM in the tangential and sagittal planes. Note that these drawings only refer to the magnification of the source. The object and its image are not represented. Note also that planes labeled “tangential focus” and “sagittal focus” refer here to the focal positions of a “virtual” point source sitting at the “object plane.”

The image distribution is given by the convolution of the ideally magnified image $[(M \times F)$, M is the magnification, F is the object distribution function] with the broadening function $[(M_{\text{src}} \times S)$ with S the source distribution function and M_{src} a magnification for the source as seen from the image]. Therefore the image distribution is $G = (M_{\text{src}} \times S) \otimes (M \times F)$, where \otimes denotes the convolution integral.

In the simplest case of the projection microscope, the image is just the projection of the object, illuminated by a quasi-point source, onto the detector plane. Here, the magnification of an object placed at a distance $(d_2 - d_1)$ from the source in an image plane at d_2 is (see Fig. 10, top)

$$M^p = d_2 / (d_2 - d_1). \quad (\text{A1})$$

The source imaged on the detector plane by a point belonging to the object (like a pin-hole camera) is magnified by a factor of

$$M_{\text{src}}^p = d_1 / (d_2 - d_1) = M^p - 1. \quad (\text{A2})$$

Using a projection microscope with the same magnification as our XCIM in the basic configuration (i.e., $M^p = M = 23.76$), one finds $M_{\text{src}}^p = 22.76$.

Now we will calculate the source magnification in the case of the XCIM in the tangential and sagittal directions. For that we consider the diameter S_i of the image at the detector plane formed by a source of diameter S_0 when a “pin-hole” camera is placed at the object position. From Fig. 10 (bottom) we obtain the values of the source magnification $M_{\text{src}} = S_i / S_0$ in the tangential and sagittal planes:

$$M_{\text{src}}^{\text{tan}} = \frac{D}{S_0} \tan \beta, \quad (\text{A3})$$

$$M_{\text{src}}^{\text{sag}} = \frac{Q' - Q - D}{S_0} \tan \gamma, \quad (\text{A4})$$

with

$$\tan \beta = S_c / Q'; \tan \gamma = S_c / Q'; S_c / S_0 = P / (p - P), \quad (\text{A5})$$

where S_c is the diameter of the source imaged at the crystal position. Therefore,

$$M_{\text{src}}^{\text{tan}} = \frac{P}{p - P} \frac{D}{Q'}, \quad (\text{A6})$$

$$M_{\text{src}}^{\text{sag}} = \frac{P}{p - P} [1 - (Q + D) / Q']. \quad (\text{A7})$$

Comparing these parameters with the ones of the XCIM we have $P = a$ and $Q + D = q + d$. By using Eqs. (3) and (4) we find, for our basic configuration, that $Q = 9.60$ cm and $Q' = -4.165$ cm. Then $D = 34.25$ cm and $M_{\text{src}}^{\text{tan}} = 7.66$, $M_{\text{src}}^{\text{sag}} = 24.75$. This explains our results:

- (1) The XCIM produces images with better spatial resolution in the tangential plane than a projection microscope. This is due to the smaller source magnification in the tangential plane.
- (2) The worst spatial resolution of the XCIM in the sagittal direction with respect to the tangential one is due to the fact that $M_s^{\text{sag}} > M_s^{\text{tan}}$.

¹X-ray Microscopy and Spectromicroscopy, edited by J. Thieme, G. Schmahl, D. Rudolph, and E. Umbach (Springer, Berlin, 1998), Part I.

²K. Yada and S. Takahashi, in X-ray Microscopy II, edited by D. Sayre, M. Howells, J. Kirz, and H. Barbach (Springer, Berlin, 1988), pp. 323–326.

³J. Kirz, C. Jacobsen, and M. Howells, Q. Rev. Biophys. **28**, 1 (1995).

⁴P. Dhez, P. Chevallier, T. B. Lucatorto, and C. Tarrío, Rev. Sci. Instrum. **70**, 1907 (1999).

⁵V. E. Coslett, A. Engstrom, and H. H. Pattee, X-ray Microscopy and Microradiography (Academic, New York, 1957).

⁶V. E. Coslett and W. C. Nixon, Nature (London) **168**, 24 (1951); X-ray Microscopy (Cambridge University, Cambridge, England, 1960).

⁷S. A. Pikuz, T. A. Shelkovenko, D. A. Hammer, A. Ya. Faenov, T. A. Pikuz, V. M. Dyakin, and V. M. Romanova, JETP Lett. **61**, 638 (1995); Y. Aglitskiy, T. Lehecka, S. Obenschain, C. Pawley, C. M. Brown, and J. Seely, Rev. Sci. Instrum. **70**, 530 (1999).

⁸E. Förster, K. Gäbel, and I. Uchmann, in X-ray Microscopy III, edited by A. Michette, G. Morrison, and C. Buckley (Springer, Berlin, 1992), pp. 202–205.

⁹M. Sanchez del Rio, A. Ya. Faenov, V. M. Dyakin, T. A. Pikuz, S. A. Pikuz, V. M. Romanova, and T. A. Shelkovenko, Phys. Scr. **55**, 735 (1997).

¹⁰P. Kirkpatrick and A. V. Baez, J. Opt. Soc. Am. **38**, 766 (1948).

¹¹M. Fraenkel, A. Ziegler, A. Ya. Faenov, and T. A. Pikuz, Phys. Scr. **59**, 246 (1999); T. A. Pikuz, A. Ya. Faenov, M. Fraenkel, A. Ziegler, F. Flora, S. Bollanti, P. Di Lazzaro, T. Letardi, A. Grilli, L. Palladini, G. Tomassetti, L. Reale, T. Limongi, and F. Bonfigli, Proc. SPIE **3767**, 67 (1999); T. A. Pikuz, A. Ya. Faenov, M. Fraenkel, A. Ziegler, F. Flora, S. Bollanti, P. Di Lazzaro, T. Letardi, A. Grilli, L. Palladini, G. Tomassetti, L. Reale, T. Limongi, F. Bonfigli, L. Alianelli, and M. Sanchez del Rio, Laser Part. Beams (accepted).

¹²M. Sanchez del Rio, M. Fraenkel, A. Ziegler, A. Ya. Faenov, and T. A. Pikuz, Rev. Sci. Instrum. **70**, 1614 (1999).

¹³C. Welnak, G.-J. Chen, and F. Cerrina, Nucl. Instrum. Methods Phys. Res. A **347**, 344 (1994).

¹⁴See any text of general optics, for instance, E. Hetch, Optics, 2nd ed. (Addison-Wesley, New York, 1987), p. 226.

- ¹⁵C. Tillmann, A. Persson, C.-G. Wahlström, S. Svanberg, and K. Herrlin, *Appl. Phys. B: Lasers Opt.* **61**, 333 (1995).
- ¹⁶B. Niemann, in *X-ray Microscopy and Spectromicroscopy*, edited by J. Thieme, G. Schmahl, D. Rudolph, and E. Umbach (Springer, Berlin, 1998), IV-45.
- ¹⁷E. Spiller, *Soft X-ray Optics* (SPIE, Bellingham, WA, 1994), Chap. 6.
- ¹⁸E. Di Fabrizio, F. Romanato, M. Gentili, S. Cabrini, B. Kaulich, J. Susini, and R. Barrett, *Nature (London)* **401**, 895 (1999).
- ¹⁹D. Weiss, G. Schneider, B. Niemann, P. Guttman, D. Pudolph, and G. Schmahl, *Ultramicroscopy* **84**, 185 (2000).
- ²⁰S. Brauer, G. B. Stephenson, and M. Sutton, *J. Synchrotron Radiat.* **2**, 163 (1995).